

Full Length Article

Plasma enhanced atomic layer deposition of crystallized gallium phosphide on Si with tri-Ethylgallium and tri-*tert*-Butylphosphine

SeongUk Yun^a, Cheng-Hsuan Kuo^b, Ping-Che Lee^a, Scott T. Ueda^b, Victor Wang^b, Harshil Kashyap^b, Aaron J. Mcleod^b, Zichen Zhang^b, Charles H. Winter^c, Andrew C. Kummel^{a,*}

^a Department of Chemistry and Biochemistry, University of California, San Diego, La Jolla, CA 92093, United States

^b Materials Science and Engineering Program, University of California, San Diego, La Jolla, CA 92093, United States

^c Department of Chemistry, Wayne State University, Detroit, MI 48202, United States



ARTICLE INFO

Keywords:

Gallium phosphide
Nucleation
Local epitaxy growth
Plasma enhanced atomic layer deposition
tri-TBP
TEGa

ABSTRACT

25 ~ 30 nm thick polycrystalline gallium phosphide (GaP) films with high P / Ga atomic ratios were deposited on Si (100) using a plasma enhanced atomic layer deposition (PE-ALD) process with triethyl gallium (TEG), tri-tertiary butyl phosphide (tri-TBP), and atomic hydrogen. The key is chemical functionalization of the Si (100) surface since the wet-cleaned Si surface is nearly inert to TEG and tri-TBP. *In-situ* Auger spectroscopy was employed to identify the most successful functionalization which employed a gas phase mixture of atomic hydrogen and tri-TBP consistent with formation of a surface phosphide layer on Si(100); this layer efficiently nucleated the PE-ALD of GaP. The crystallinity and surface roughness of GaP films were tuned by controlling the pulse length of atomic H plasma, showing the self-limiting ALD film growth with 2.7 Å/cycle. The optimal crystallized GaP thin film on 6°-miscut Si showed local epitaxy growth of homogeneous GaP *epi*-layers in transmission electron microscopy (TEM).

1. Introduction

Crystallized gallium phosphide (GaP) epitaxially grown on silicon (Si) has recently gained significant interest in optoelectronics, X-ray multi-layer mirrors [1], and III-V semiconductor heterostructures because of its high refractive index and low band-gap [2,3]. GaP being a III-V semiconductor with an indirect band gap of 2.26 eV and having a lattice mismatch with Si of less than 0.36 % could be employed as a nucleation layer and buffer layer for further growth of III-V compounds or as a window/emitter layer for Si-based optoelectronics [2].

For growth of GaP on Si(100), the nucleation is critical since wet cleaned Si(100) is nearly inert to common Ga and P precursors. The nucleation process for GaP growth on Si has previously been studied using metal-organic chemical vapor deposition (MOCVD) [4] or molecular beam epitaxy (MBE) [5]. Beyer et al. suggested that the GaP polarity could be modified on as-grown buffer Si layer at 975 °C by controlling nucleation for GaP MOCVD process [4]. The low nucleation density leads to the different directions of epitaxial growth and, therefore, a high density of grain boundaries [6,7]. For all CVD and ALD growth techniques, a high-quality and reliable nucleation process at low

temperature is crucial to maximize the nucleation density and minimize nucleation-related defects such as micro-twins (MTs), antiphase domains (APDs), stacking faults (SFs), and achieve low threading dislocation density (TDD).

High toxicity phosphine (PH₃) and high vapor pressure trimethylgallium (TMGa) are the typical phosphorus and gallium precursors to study GaP thin film growth using conventional thermal chemical vapor deposition (CVD) processes [8]. However, the deposited GaP films require an extremely high flow ratio of phosphorus to gallium precursors [9]. In addition, the high toxicity of PH₃ and the high vapor pressure of TMGa inhibit comprehensive research on the initial nucleation and growth mechanism of this process. Grassman et al. reported defect-free thin GaP film deposition using molecular beam epitaxy (MBE) as a templating layer for CVD with triethylgallium (TEGa) and mono-*tert*-butylphosphine (mono-TBP) which is highly toxic and has high vapor pressure [5]. However, a GaP ALD process has not yet been reported using TEGa and safer tri-*tert*-butylphosphine (tri-TBP) since the tri-TBP needs a high temperature to be reactive on Si (100), whereas the TEGa is easily decomposed on GaAs (100) above 300 °C [10]. The tri-TBP could be the optimal phosphorous precursor for toxicity and

* Corresponding author.

E-mail address: akummel@ucsd.edu (A.C. Kummel).

<https://doi.org/10.1016/j.apsusc.2023.156727>

Received 28 October 2022; Received in revised form 4 February 2023; Accepted 10 February 2023

Available online 14 February 2023

0169-4332/© 2023 Elsevier B.V. All rights reserved.

vapor pressure. Therefore, it is highly desirable to develop the low-temperature growth of crystallized GaP thin film on Si substrate using the safe tri-TBP precursor and TEGa precursor.

There are two reports of chemical templating of Si for the growth of GaP. Boyer et al. recently reported that mono-TBP (a highly toxic compound) initiated atomic layer epitaxy (ALE) on Si(100) substrate at 450 °C effectively decreased the nucleation-related defects [11] and Gudovskikh et al. reported obtaining microcrystalline GaP on Si(100) substrate at low temperature (~380 °C) by using a PE-ALD-like method with a continuous atomic H plasma with PH₃ (an extremely toxic gas) and TMGa (a high vapor pressure precursor) [12]. The use of plasma chemistry without the use of toxic mono-TBP nor PH₃ for nucleation of local epitaxy growth could be a promising alternative technique due to the improved reactivity and uniformity of radical reactions with Si surfaces. However, the impact of tri-TBP dry-clean on GaP nucleation has not been widely studied for GaP growth on Si.

A variety of growth methods have been studied to achieve GaP growth on Si, including molecular beam epitaxy (MBE), metal-organic chemical vapor deposition (MOCVD), hydride vapor phase epitaxy, and plasma-enhanced atomic layer deposition (PE-ALD) [13–19]. The MOVPE [20] and MBE [16] were previously proposed to improve the crystalline properties of the GaP. However, high temperatures (≥ 600 °C) are required to use these techniques on Si substrates. The high-temperature processes for Si substrates led to unintentional deoxidation and reconstruction on the Si surface during epitaxial GaP growth, resulting in a negative impact on the efficiency of optoelectronic devices on Si substrate due to a significant decrease in the lifetime of minority charge carriers in the Si substrate [21]. In general, applying a typical Ar⁺, atomic H, or NH₄⁺ ion bombardment using a plasma source during epitaxy growth may overcome the challenges of high-temperature processing and low precursor reactivity for epitaxial III–V semiconductors on Si [22,23]. Plasma-enhanced atomic layer deposition (PEALD) has been reported to show several advantages relative to thermal ALD: homogenous high-quality thin-film deposition on large areas, enhancing the overall process efficiency, and low temperature process by plasma stimulation instead of just using thermal energy [24] which is especially beneficial for optoelectronic applications of thin-film fabrication on Si.

Ueda et al. showed that using atomic layer annealing (ALA) improved the crystalline quality of the epitaxy layers of III–V compounds (aluminum nitride) at low temperature as compared to the conventional thermal ALD [25]. Gudovskikh et al. reported the possibility to obtain microcrystalline GaP on Si at low temperature (~380 °C) by using a PE-ALD-like method with a continuous atomic H plasma with PH₃ and TMGa [12]. Uvarov et al. reported recently that the thin epitaxial GaP layers were grown on Si using PE-ALD with PH₃ and TMGa at temperatures below 400 °C using an additional ALD pulse of Ar plasma without DC bias [26].

Four functionalization/nucleation methods were investigated in this study for the ALD process of GaP films on Si (100) substrates; thermal ALD cycles of tri-TBP and TEGa, pre-pulse of TEGa, pre-pulse of tri-TBP, and tri-TBP dry-clean with atomic H plasma. PE-ALD was investigated for formation of high-quality polycrystalline and crystalline GaP films on Si (100) substrates after functionalization. The PE-ALD technique is denoted as the atomic H ALD in this study since the plasma process employed atomic H as an individual pulse in each ALD cycle. The potential growth mechanism of GaP atomic H ALD on Si is proposed. Understanding the growth mechanism and nucleation process of GaP layer is essential to enabling mass production of epitaxial GaP and further development of III–V semiconductors on Si. Lastly, local epitaxy growth of crystallized GaP *epi*-layer was successfully achieved by using the 6°-miscut Si substrate. This is the first report of low-temperature growth of crystallized GaP by ALD on Si(100) using tri-TBP and TEGa.

2. Experimental methods

Materials. GaP atomic H ALD thin films were prepared by plasma

enhanced ALD process with tri-ethylgallium (TEGa) provided by EMD performance materials and tri-*tert*-butylphosphine (tri-TBP) purchased from Strem chemicals. 6 mm × 12 mm of pre-diced *n*-type Si (100) with a resistivity of 1–10 Ω·cm were employed as substrates; the 100 mm diameter Si wafers were purchased from Universitywafer. ACS Regents grade of acetone (99.5 + wt.%), methanol (99.5 + wt.%), deionized (DI) water (99.5 + wt.%), and hydrofluoric (HF) acid (48 wt.%) were purchased from Fisher Scientific. Ultra-high purity (UHP) grade of Ar (99.999 vol%) was purchased from Praxair and purified using an Entegris Gatekeeper gas purifier for use as a purge gas for the ALD process.

Si substrate preparation. 6 mm × 12 mm of pre-diced Si (100) samples were degreased by rinsing with acetone, methanol, and DI water, sequentially. The native Si oxide after degreasing step was etched by dipping in HF diluted solution of 2 wt.% in DI water for 2 min. The samples were immediately loaded onto the vacuum chamber with a copper sample holder. After pumping the isolated loading chamber down to a pressure below 2×10^{-6} Torr, the samples were transferred to the ALD process chamber.

Thin film preparation. The custom ALD process chamber was pumped by a commercial dry pump (Edwards EPX-500NE). A liquid nitrogen cold trap and stainless-steel mesh were installed between the ALD process chamber and the dry pump to minimize the impurities and moisture and to collect excess precursors and particulates. The ALD process was performed at 90 °C chamber wall temperature with a base pressure below 2.0×10^{-6} Torr.

The sample stage in the ALD chamber was made of an electrically isolated copper block heated by a cartridge heater. Pneumatically actuated diaphragm ALD valves were installed and tri-TBP was dosed at 60 °C bottle temperature without carrier gas. Multiple doses of tri-TBP were employed to deliver a larger amount of precursor than a single dose of long pulse length to limit the maximum pressure on the drag pump. Gas flows to the plasma were controlled by mass flow controllers and fed into a RF remote plasma source (PIE Scientific) with a sapphire plasma tube mounted above the chamber. Note the gasses continue to flow through the plasma source when the plasma is not ignited thereby acting as a typical ALD purge gas. The atomic H plasma used a 0–20 s plasma treatment each cycle at a power of 75 W using 10 mTorr of Ar and 40 mTorr of H₂ mixture without stage DC bias. The samples are denoted as GaP *n* s atomic H ALD, where *n* stands for the pulse length of atomic H plasma as an additional ALD pulse. It is noted that the Ar in the plasma gas will form Ar⁺ which will contribute to the crystallinity of the GaP as shown by Ueda [25].

***In-situ* Auger Electron Spectroscopy (AES).** Chemical composition was estimated by *in-situ* AES using a micro-cylindrical mirror Auger spectrometer (micro CMA, RBD Instruments). The as-deposited samples were transported *in-vacuo* to an attached auger chamber (base pressure below 1×10^{-8} Torr). The microCMA Auger spectrometer scanned a kinetic energy range of 40–1500 eV with a step size of 1 eV. The beam potential was 3 kV with a filament current of 0.88 A. The AES results were collected and processed using CMapp software (RBD Instruments).

Transmission Electron Microscopy. The lamella for the cross-sectional *epi*-layer image was prepared on a Thermo-Fisher (FEI) Helios UC FIB-SEM at Covalent Metrology. High-resolution transmission electron microscopy (HR-TEM) and scanning transmission electron microscopy (STEM) imaging were performed on a Thermo-Fisher (FEI) Talos F200X G2 with a bright XFEG source and a high angle annular dark field (HAADF) detector. EDS was measured on a Thermo-Fisher (FEI) Super X EDS detector during their HAADF-STEM analysis. The chemical compositions of GaP films on Si were determined by converting raw EDS counts in EDS mapping using the Velox software. Selected area electron diffraction patterns were obtained by fast Fourier transform (FFT) of HR-TEM images using Gatan Microscopy Suites (GMS) software.

Atomic Force Microscopy (AFM). The surface morphology was investigated with a Veeco Scanning Probe Microscope equipped with a Nanoscope IV controller (Veeco Instruments, Woodbury, NY, USA).

Non-coated Si AFM probes and 15 mm diameter of sample specimen discs, purchased from Ted Pella Inc., were employed in tapping mode analysis. The $2\ \mu\text{m} \times 2\ \mu\text{m}$ of AFM images were determined by Gwyddion 2.60 scanning probe microscope (SPM) software.

Grazing Incidence X-ray Diffractometry (GI-XRD). Crystallinity and crystalline patterns of *epi*-layers were identified by Rigaku Smartlab diffractometer performed GI-XRD with Cu K α source ($\lambda = 1.5418\ \text{\AA}$) operating at 40 kV. X-ray reflectivity (XRR) was analyzed on the same diffractometer with the Smartlab studio software suite (Rigaku).

Spectroscopic Ellipsometry (SE). The thickness of GaP films was estimated using a spectroscopic ellipsometer (model M-2000D, J.A. Woollam Co., Inc.) equipped with a focusing probe that reduced the spot size to 300–400 μm . The SE results were collected at incident angles of 75° . The SE data were fit with a transparent oxide film (GaP) on Si substrate using CompleteEase (J.A Woollam Co., Inc.) software.

3. Results and discussion

Fig. 1 shows the sequence of the ALD pulse switching during the GaP atomic H ALD growth process. The stage temperature of ALD chamber was increased up to $500\ ^\circ\text{C}$ under ultra-high vacuum pressure for 40 min before the ALD process. The 75 W remote RF plasma was employed for 3 min with 10 mTorr of Ar and 40 mTorr of H_2 gas as shown in Fig. 1. The 13 cycles of tri-TBP pulses were introduced into the ALD chamber after 30 s of plasma ignition as a nucleation step. After 3 min nucleation of tri-TBP dry-clean, 3×800 ms of tri-TBP were dosed without plasma stimulation to nucleate the Si surface with phosphide functional groups. The ALD process cycles began on the functionalized Si substrate with 10 mTorr of Ar and 40 mTorr of H_2 . For ALD process cycles, TEGa was dosed as a first ALD pulse, atomic H plasma was employed as a second ALD pulse without precursor dosing, and tri-TBP was dosed as a third ALD pulse. (a)–(e) in Fig. 1 indicate that *in-situ* AES analysis was performed for each ALD pulse and the chemical compositions will be discussed below.

Fig. 2 shows the chemical compositions over four different nucleation methods followed by the 100 cycles of GaP atomic H ALD process. Four different nucleation methods were performed at $500\ ^\circ\text{C}$ of stage temperature in 50 mTorr chamber pressure with $\text{H}_2 + \text{Ar}$ mixture: “Thermal ALD pre-cycle” was 50 cycles of typical thermal ALD process with 200 ms of TEGa, 5 s purge, 3×800 ms of tri-TBP, and 5 s purge; “tri-TBP only pre-pulse” was 50 pulses of 3×800 ms of tri-TBP with 5 s purge; “TEGa only pre-pulse” is 40 pulses of 200 ms of TEGa with 5 s purge; “tri-TBP dry-clean” was 13 pulses of 3×800 ms of tri-TBP with 5 s purge with 75 W H_2 plasma.

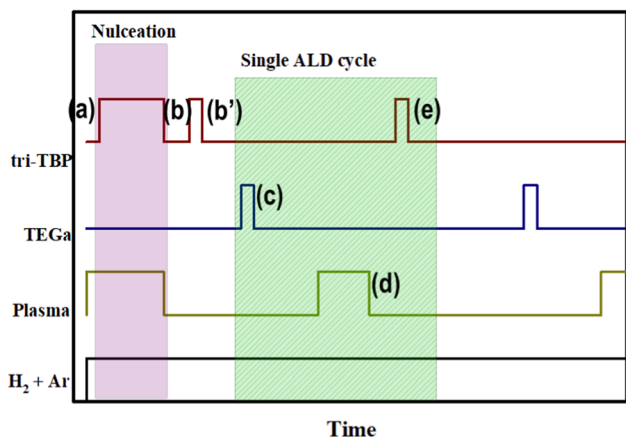


Fig. 1. ALD pulse switching diagram for the growth of GaP atomic H ALD. Intensity of y-axis illustrates pulse on/off regardless of pressure or intensity, time of x-axis displays only sequence does not represent the specific pulse length. (a)–(e) indicates when *in-situ* AES analysis was performed for each ALD pulse and chemical compositions from these AES are shown below.

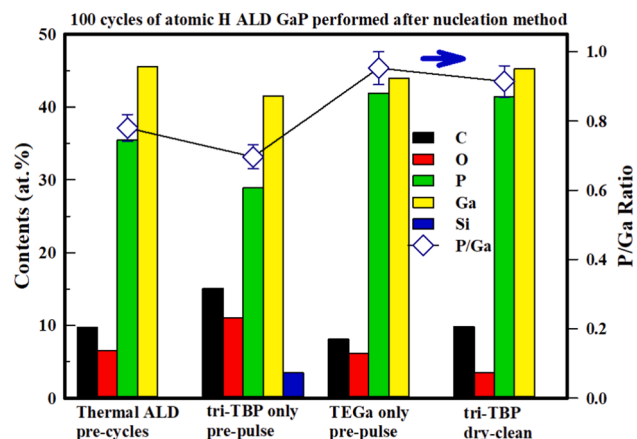


Fig. 2. In-Situ AES of four Nucleation Techniques. Chemical compositions of the as-deposited 100 cycles of GaP atomic H ALD on Si using *in-situ* auger electron spectroscopy after four different nucleation methods; thermal ALD pre-cycles, tri-TBP only pre-pulse, TEGa only pre-pulse, and tri-TBP dry-clean.

The 3.5 at.% of Si content after nucleation of tri-TBP only pre-pulse plus 100 GaP ALD cycles indicated an extremely low growth rate of GaP film on Si (100). Although the Si signal for AES of thermal ALD pre-cycles nucleation plus 100 GaP ALD cycles disappeared, the low P/Ga atomic ratio suggested the formation of a poor-quality GaP film. In addition to chemical composition, extremely rough surface morphology was observed in both nucleation methods of thermal ALD pre-cycle and tri-TBP only pre-pulse (not shown) plus 100 GaP ALD cycles, indicating a significant CVD process instead of ALD local epitaxial growth.

The TEGa only pre-pulse and tri-TBP dry-clean plus 100 GaP ALD cycles showed high P/Ga atomic ratios (≥ 0.92) and low oxygen contents (≤ 3.8 at.%). The P/Ga atomic ratios of TEGa only pre-pulse and tri-TBP dry clean in Fig. 2 (0.95 ± 0.04 and 0.92 ± 0.04) are similar and high compared to the ratios from the other two nucleation methods. The AFM images of the TEGa only pre-pulse and tri-TBP dry-clean plus 100 GaP ALD cycles are shown in Figure S1. Smooth surface morphology (RMS = 1.5) was observed for tri-TBP dry-clean nucleation, while the TEGa only pre-pulse had rough surface morphology (RMS = 3.4 nm). The rough surface morphology of TEGa only pre-pulse could result from the island growth due to its low nucleation density consistent with the low reactivity of thermal TEGa. This observation suggests that tri-TBP dry-clean is the best nucleation method for the atomic H ALD GaP process which is further confirmed by cross-sectional transmission electron microscopy analysis shown below.

The optimization study of GaP atomic H ALD tri-TBP dry-cleaned Si (100) is shown in supporting information (Figure S2–S5). The atomic H plasma pulse length of 10 s and 15 s showed higher phosphorus contents (P/Ga atomic ratios = 0.95 and 0.92) and lower O impurity contents (3.8 at.% and 3.5 at.%) for the GaP atomic H ALD on Si than those of insufficient or excess (5 s or 20 s) atomic H. The smoothest surface morphology (RMS = 1.5 nm) was observed in the GaP 15 s atomic H ALD on Si, but most GaP *n* s atomic H ALD films on Si showed smooth surface morphology (RMS = 1.5 ~ 2.4 nm) except for GaP 20 s atomic H ALD on Si (RMS = 3.4 nm). The average crystallite size of GaP (111) determined by Scherrer’s equation [27] using XRD patterns as a function of atomic H plasma pulse increased continuously, while GaP 20 s atomic H ALD on Si showed a rough surface morphology and faster growth rate than one monolayer per cycle due to the etching of the excess atomic H plasma. In addition, the growth rate per cycle as a function of TEGa and tri-TBP was saturated at 100 ms of TEGa and 4×400 ms of tri-TBP, respectively, indicating self-limiting ALD film growth within the ALD GPC regime (2.7 $\text{\AA}/\text{cycle}$).

Fig. 3 shows the cross-sectional *epi*-layer image of GaP atomic H ALD on Si after the nucleation of TEGa only pre-pulse. The blurry region of

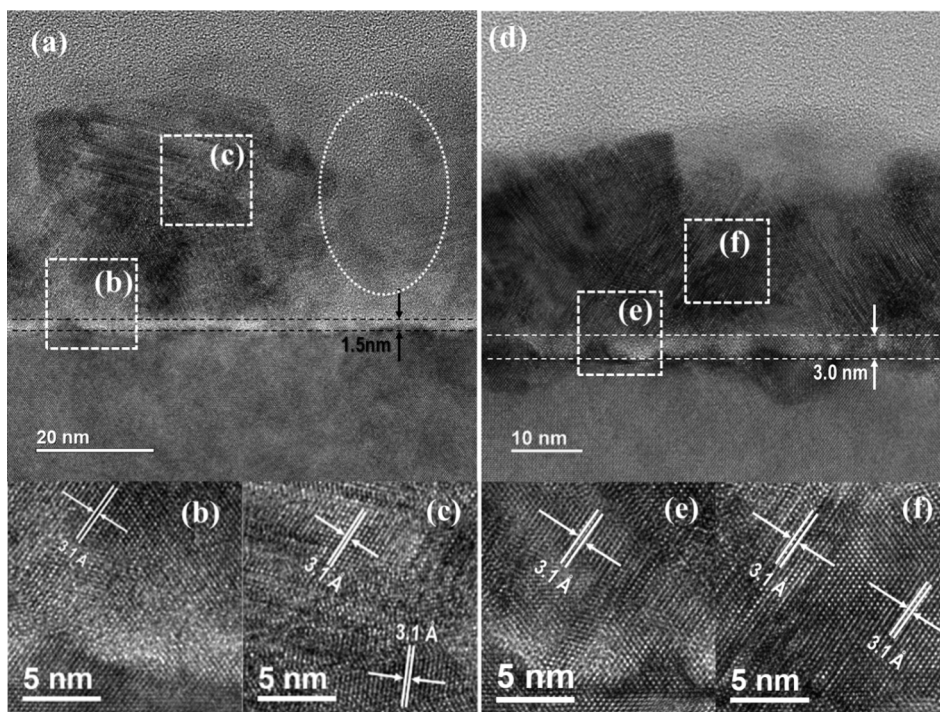


Fig. 3. HR-TEM images of (a-c) GaP atomic H ALD on TEGa only pre-pulsed Si and (d-f) GaP atomic H ALD on tri-TBP dry-cleaned Si. Local epitaxy growth of GaP (111) with lattice fringe (3.1 Å) at dark region in HR-TEM images of the TEGa only pre-pulse nucleation (a-c) and Homogeneous deposition of GaP *epi*-layer with lattice fringe (3.1 Å) of GaP (111) in the HR-TEM images of tri-TBP dry-clean nucleation (d-f).

the white circle in Fig. 3a suggested the presence of a less dense GaP film and amorphous-like, or randomly oriented micro-grains of GaP species as compared to the other regions with dark contrast in the crystallized GaP films. Distinct local epitaxy growth of GaP on Si was observed in the interfacial layers (Fig. 3b) and the region of dark contrast in Fig. 3a. A 3.1 Å lattice fringe, corresponding to the spacing of (111) plane of GaP,

was observed in Fig. 3b and 3c, while different directions of GaP film growth were observed in Fig. 3c. The unevenly distributed dark contrast and columnar white circle in the GaP film in HR-TEM images indicate the heterogeneous growth of GaP film, which could be attributed to the low nucleation density from the TEGa pre-pulse.

High angles angular dark field (HAADF) STEM image and

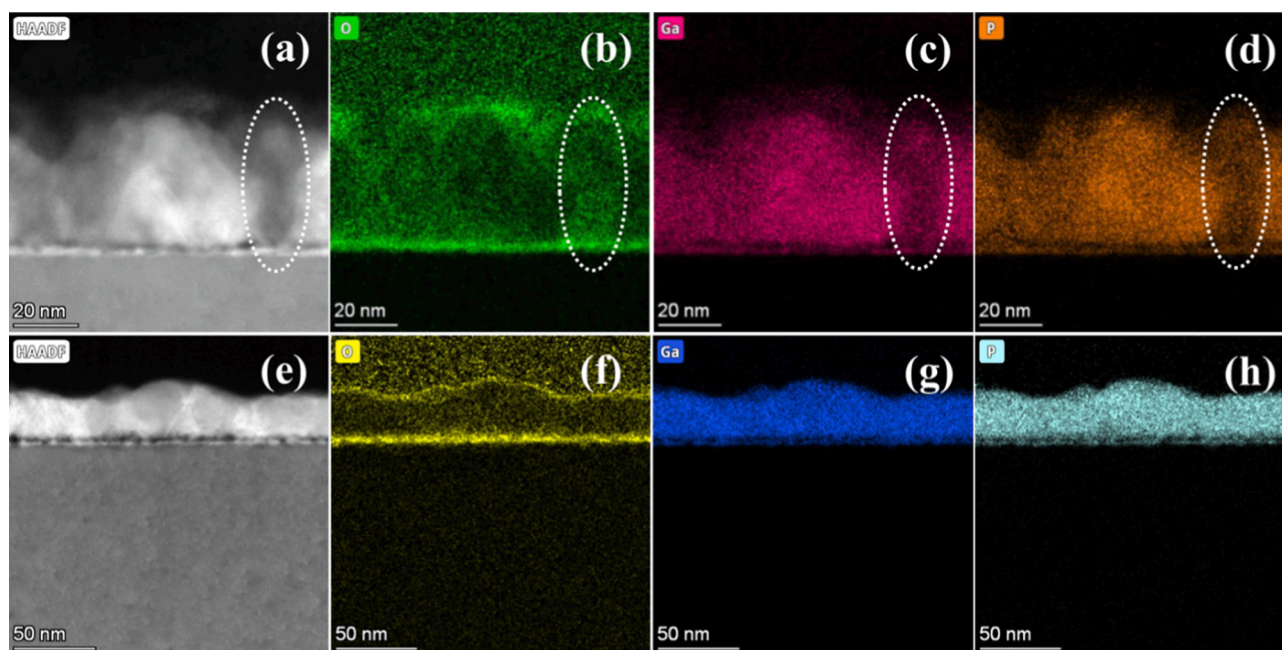


Fig. 4. Effect of Nucleation Method on Interface Structure and Composition of GaP Atomic H ALD. HAADF-STEM image and EDS maps of (O, Ga, and P) of GaP Atomic H ALD on (a-d) TEGa only pre-pulsed vs GaP Atomic H ALD on tri-TBP dry-cleaned Si. (a-d) Heterogeneous GaP film growth with high oxygen content at white circles in HAADF-STEM and EDS maps are shown in the TEGa only pre-pulse nucleation. (e-f) Uniform chemical distribution with low oxygen impurity is shown in HAADF-STEM and EDS maps of the tri-TBP dry-clean nucleation.

corresponding energy-dispersive X-rays (EDS) maps of oxygen, gallium, and phosphorus over the nucleation of TEGa only pre-pulse are shown in Fig. 4(a-d), respectively. The dark contrast of the columnar white circle in HAADF-STEM image (Fig. 4a) suggests lower density and/or reduced crystallinity/non-stoichiometric GaP film as compared to the crystallized GaP layers (brighter contrast). The white circles in the EDS maps of the TEGa nucleated atomic GaP/Si indicated higher O and lower Ga and P content in the low nucleation region and agreed with the partial formation of oxidized GaP species at the Si surface (white circles). These observations suggest that the nucleation of TEGa only pre-pulse was insufficient to activate uniformly the Si surface despite the observation of local epitaxy growth at the limited region of the Si surface with high nucleation density.

Fig. 3d-f shows the HR-TEM images of GaP atomic H ALD on Si after the nucleation of tri-TBP dry-clean. The uniformly distributed dark contrast in GaP *epi*-layers and the bright region between two white dotted lines in Fig. 3d indicate a homogeneously deposited GaP *epi*-layer and oxygen-rich interfacial layers, respectively. The dark contrast in HR-TEM was attributed to the denser and/or better crystallized/oriented GaP crystallites than lighter contrast oxygen-rich interfacial layers. Fig. 3e and 3f illustrate the presence of 3.1 Å lattice fringe in the GaP film, which corresponds to the (111) d-spacing of GaP. Furthermore, local epitaxy growth of GaP was observed near the entire interfacial layer consistent with the small lattice mismatch between GaP *epi*-layers and Si substrate.

Fig. 4e-f display the HAADF-STEM image and EDS maps of GaP atomic H ALD on tri-TBP dry-cleaned Si. The HAADF-STEM image (Fig. 4e) demonstrates a more uniform Z contrast of the *epi*-layers, indicating uniformly crystallized GaP film growth. The uniform distribution of chemical composition in ALD thin films has been widely studied using EDS maps with HAADF-STEM imaging [28]. Alqahtani et al. reported uniformly deposited GaP with low oxygen content in GaP thin film using EDS maps with HAADF-STEM image [29]. The EDS map of oxygen (Fig. 4f) shows low oxygen impurity content in the GaP films despite ex-situ TEM analysis after lamella preparation for cross-sectional *epi*-layer imaging. The uniform distribution of gallium and phosphorus is shown in the EDS maps (Fig. 4g and 4h), indicating homogeneous GaP film growth in good agreement with the HR-TEM image (Fig. 3d-f).

The relatively uneven interfacial layers were observed in the nucleation of tri-TBP dry-clean (Fig. 3e) as compared to those in the nucleation of TEGa only pre-pulse (Fig. 3a). The atomic H plasma could etch the Si surface during the tri-TBP dry-clean due to high substrate temperature at 500 °C. In addition, residual gallium precursor could have

diffused into the Si surface layer by the undesirable reaction of Ga and Si, so-called melt-back etching [30,31]. It could be hypothesized that GaP atomic H ALD process at 500 °C could lead to melt-back etching, further study might be needed to elucidate the mechanism.

The proposed growth mechanism for GaP 15 s atomic H ALD is shown in Fig. 5 based on the HR-TEM, *in-situ* AES, XRD, AFM, and thickness studies. During the wet-clean preparation step of the Si substrate, the native oxide of Si (100) substrate was effectively removed by dipping the Si substrate in a 2 wt.% HF aqueous solution and converting it to H-terminated Si (Fig. 5a and Fig. 6a). The H-terminated Si has very low reactivity toward the ALD precursors. In the nucleation step, 13 pulses of 3×800 ms of tri-TBP were introduced into the ALD chamber simultaneously with atomic H plasma at 500 °C for 3 min. It is proposed that the tri-TBP precursor can be partially decomposed to $\text{PH}(\text{C}_4\text{H}_9)_2$, $\text{PH}_2(\text{C}_4\text{H}_9)$, or PH_3 since mono-TBP was reported to decompose thermally above 320 °C to $\text{PH}_3 + (\text{C}_4\text{H}_8)^+$ above 320 °C [32]. It is hypothesized that Si-H could be deprotonated by abundant atomic H and functionalized to $\text{SiP}(\text{C}_4\text{H}_9)$ by reacting with $\text{PH}_2(\text{C}_4\text{H}_9)$. This tri-TBP dry-clean enables the non-polar Si-H to convert to the polar nucleation layer of $\text{Si-PH}(\text{C}_4\text{H}_9)$ (Fig. 5b). The increased phosphorus content and the atomic ratio of surface carbon to Si substrate after tri-TBP dry-clean were evident in *in-situ* AES as shown in Fig. 6b.

After the nucleation process was completed, 3×800 ms of tri-TBP was dosed on the Si substrate at 500 °C as a passivation step to fully functionalize the Si surface with the phosphide functional group. After 10 s of the purge process, a single 200 ms of TEGa pulse was injected as the first ALD pulse. It is hypothesized that the injected $\text{Ga}(\text{C}_2\text{H}_5)_3$ (TEGa) could react with P-H site of the functionalized $\text{Si-PH}(\text{C}_4\text{H}_9)$ which is demonstrated in Fig. 5c. The TEGa precursor was reported to thermally decompose above 350 °C [10] and it is proposed that the partially decomposed $\text{GaH}(\text{C}_2\text{H}_5)_2$ could react with P-H sites since P-H bond (343 kJ/mol) is weaker than P-C bond (513 kJ/mol) [33]. Furthermore, the reported pKa value of CH_2H_6 , H_2 , and P-H (PH_3) were ~ 50 , ~ 35 , and ~ 27 , respectively [34-36]. It could be thermodynamically favorable to deprotonate from P-H bonds on the surface by $\text{GaH}(\text{C}_2\text{H}_5)_2$ since the ethyl groups should be more readily accept protons than P-H bonds. The increased Ga content and the atomic ratio of surface carbon to Si substrate observed by *in-situ* AES after TEGa pulse (Fig. 6c) are consistent with this proposed reaction pathway.

The second ALD pulse was introduced with 15 s of atomic H plasma after 10 s of purge time. During the atomic H plasma pulse, it is proposed that the organic ligands ($-\text{C}_2\text{H}_5$ and $-\text{C}_4\text{H}_9$) were effectively removed by the atomic H plasma and induced the formation of a crystallized Ga-P

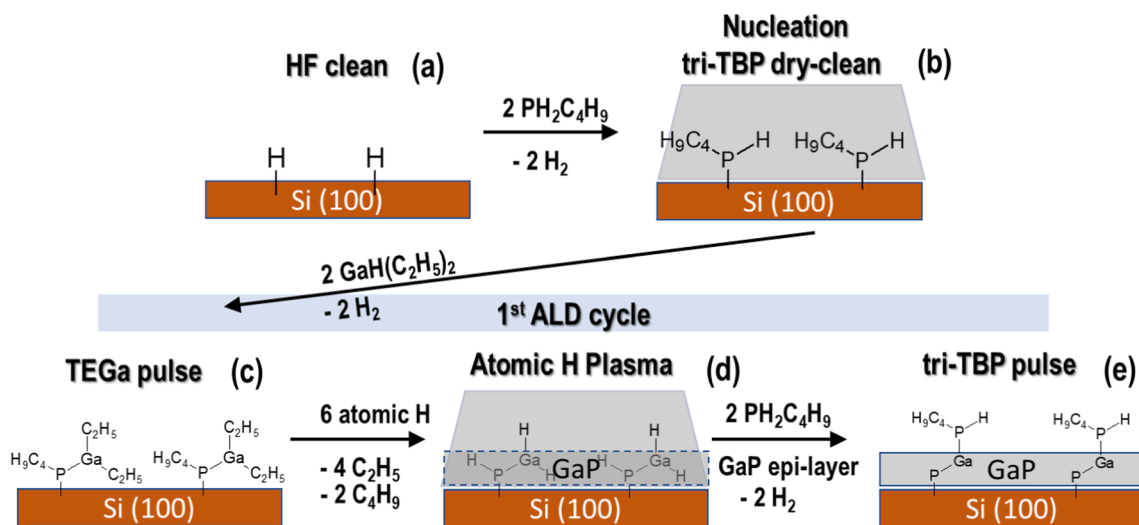


Fig. 5. Proposed mechanism of GaP Nucleation and GaP atomic H ALD growth. Proposed nucleation mechanism for phosphide functionalization on Si (100) substrate using tri-TBP dry-clean and growth mechanism of GaP atomic H ALD.

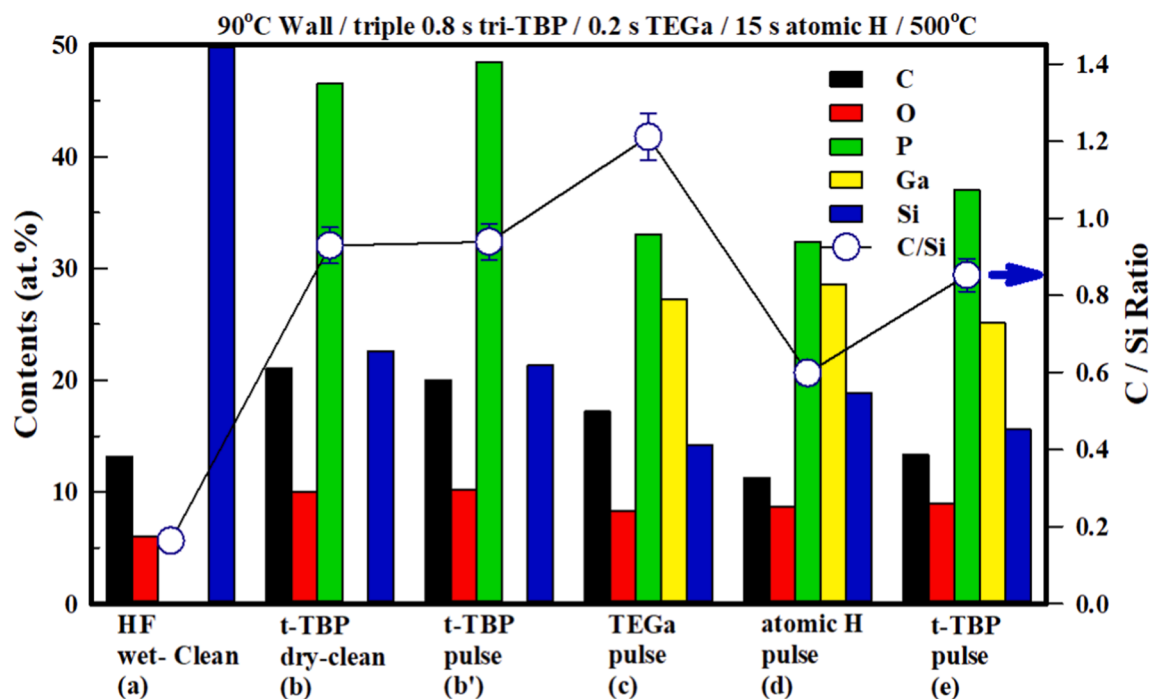


Fig. 6. *In-situ* AES of each step for the GaP 15 s atomic H ALD process. Chemical compositions over the sequential six steps for single Si substrates *in vacuo*; (a) HF clean Si, (b) tri-TBP dry clean (nucleation), (b') tri-TBP pulse without plasma stimulation (passivation), (c) TEGa pulse (first ALD pulse), (d) atomic H pulse (second ALD pulse), and (e) tri-TBP pulse (third ALD pulse).

epi-layer (Fig. 5d). The removal of organic ligands from TEGa using hydrogen plasma was previously reported [37]. The decreased atomic ratio of carbon to silicon (Fig. 6d) after the atomic H plasma pulse observed by *in-situ* AES and the enhanced growth rate and crystallinity (Figure S3 and Fig. S5(d)) as a function of atomic H plasma length also support this suggested reaction pathway.

Lastly, 3×800 ms of tri-TBP was introduced as a third ALD pulse. *In-situ* Auger spectroscopy (Fig. 6e) showed increased carbon and phosphorus content after the tri-TBP pulse as the third ALD pulse. This suggests that the partially decomposed $\text{PH}(\text{C}_4\text{H}_9)_2$ from tri-TBP at 500 °C [32] was reacted with Ga-H terminating sites of as-deposited GaP *epi*-layer, which converted to the Ga-PH(C_4H_9) layer and the functionalized P-H sites would be reacted with next TEGa pulse for the next ALD cycle (Fig. 5e). During the ALD process, the P-H bonds and Ga-H bonds other than the topmost terminating Ga-H bonds could be converted to an ordered Ga-P *epi*-layer. Based on the proposed growth mechanism, high-quality crystallized GaP ALD film was deposited on tri-TBP dry-cleaned Si (100) using the atomic H ALD process at 500 °C

using the safer TEGa and tri-TBP precursors. The mechanism scheme for the extended ALD cycles (first two ALD cycles) and reaction pathways are demonstrated in Figure S14. Figure S15 shows the mechanism scheme with an assumption that tri-TBP ($\text{P}(\text{C}_4\text{H}_9)_3$) was fully decomposed to phosphine (PH_3) at a 500 °C stage temperature.

Fig. 7 shows the transmission electron microscopy images of cross-sectional GaP *epi*-layers of GaP atomic H ALD on (a) Si without miscut and (b) 6°-miscut Si. Fig. 7a demonstrates the local epitaxial growth of GaP *epi*-layers on the entire surface of Si without miscut. The discrete contrast difference due to the domain misorientation and tentative grain boundaries (marked in red lines) were observed in Fig. 7a. The digital diffraction patterns of the selected area were obtained by fast Fourier transform (FFT) of HR-TEM images using Gatan Microscopy Suites (GMS) software. Three of six digital diffraction patterns in Fig. S6e-g are inconsistent with that of Si substrate orientation (Fig. S6b), suggesting domain misorientation and ring-pattern of diffraction of GaP. Although the tri-TBP dry-clean significantly improved the functionalization of Si surface and enable the deposition of homogeneous GaP ALD film

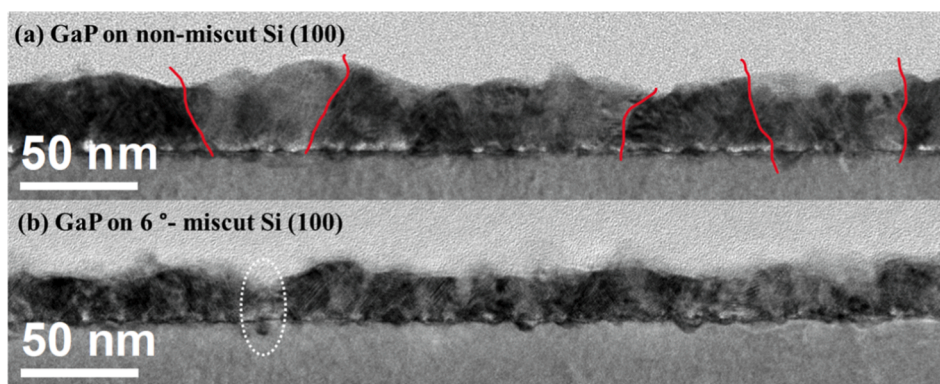


Fig. 7. Low magnification TEM images of GaP 15 s atomic H ALD on Si (100) and 6° miscut Si (100). Discrete domain boundaries (red lines) observed in GaP atomic H ALD on (a) non-miscut Si(100) and local epitaxy growth observed in GaP atomic H ALD on (b) miscut Si (100) without distinct domain boundaries. (For interpretation of the references to colour in this figure legend, the reader is referred to the web version of this article.)

growth, the domain size could be suppressed by surface anti-phase domains due to the polar GaP local epitaxial growth on the non-polar Si substrate [38]. However, miscut Si substrate may overcome these challenges since most anti-phase domain could be self-annihilated by the spontaneously nucleated domains with the broken symmetry of miscut substrate. [39,40].

HR-TEM images and selected area electron digital diffraction patterns of GaP Atomic H ALD on 6°-miscut Si were analyzed to identify the local epitaxy growth near interface layer. Several digital diffraction patterns near interfacial layers were obtained from two individual rHR-TEM images (Figs. 8 and S7) of GaP atomic H ALD on 6°-miscut Si. Three digital diffraction patterns in 10 nm × 10 nm of selected areas in each HR-TEM image showed essentially the same orientations (white and black circles) of Si as shown in Fig. 8b-e and S7b-e. A distance of 3.1 Å between diffraction pattern and center in digital diffraction pattern was determined by GMS software in both Si substrate and GaP *epi*-layers, which corresponds to the (111) d-spacing of GaP and Si. These observations suggest the local epitaxy growth of GaP *epi*-layers on 6°-miscut Si substrate. In addition, Fig. 7b shows transmission electron microscopy images of cross-sectional GaP *epi*-layers of GaP atomic H ALD on 6°-miscut Si. The clean line shape diffraction patterns of GaP *epi*-layers without ring-patterns in the digital diffraction patterns (Fig. 8b-e and S7b-e) and the absence of distinct domain boundaries in Fig. 7b also suggest local epitaxial growth of GaP *epi*-layers. The relatively thin GaP films of the white dotted circle in Fig. 7b might be attributed to the variation of TEM analysis from the mis-alignment of TEM lamella and low nucleation density.

4. Conclusions

Local epitaxial growth of GaP on Si with a high P/Ga atomic ratio and smooth surface morphology was prepared by atomic H plasma-enhanced ALD process by controlling the pulse length of atomic H plasma using tri-TBP dry-cleaned Si substrate. The atomic H plasma used a 0–20 s plasma treatment each cycle at a power of 75 W using 10 mTorr of Ar and 40 mTorr of H₂ mixture without stage DC bias. Four functionalization/nucleation methods were investigated; thermal ALD cycles of tri-TBP and TEGa, pre-pulse of TEGa, pre-pulse of tri-TBP, and tri-TBP dry-clean with atomic H plasma. The nucleation process using the tri-TBP dry-clean showed the most homogeneous nucleation because it functionalizes the surface with phosphorus. The mechanisms of nucleation and reaction path-way of GaP atomic H ALD were proposed. The 15 s atomic H plasma as an ALD pulse is critical to gain high quality of GaP *epi*-layers; however, the use of atomic H plasma makes an inevitable trade-off between facilitating the formation of ordered GaP species by removing carbon impurities and detrimental etching which may also induce formation of disordered GaP. Both insufficient carbon removal and etching of GaP are hypothesized to make the GaP film or surface amorphous and, therefore, susceptible to oxidation by trace H₂O in the ALD chamber. Therefore, the length of atomic H plasma plays a key role in the formation of highly ordered GaP layers with low oxygen content. Self-limiting ALD film growth (2.7 Å/cycle) was achieved by optimizing the GaP atomic H ALD process. Finally, ~20 nm of local epitaxy growth of GaP *epi*-layers were successfully deposited using 6°-miscut Si (100) substrate with safe tri-TBP precursor which was confirmed by HR-TEM images and digital electron diffraction patterns from FFT. It is desirable for applying the atomic H plasma-enhanced ALD process to the further development of III-V semiconductors on Si substrate.

Declaration of Competing Interest

The authors declare that they have no known competing financial interests or personal relationships that could have appeared to influence the work reported in this paper.

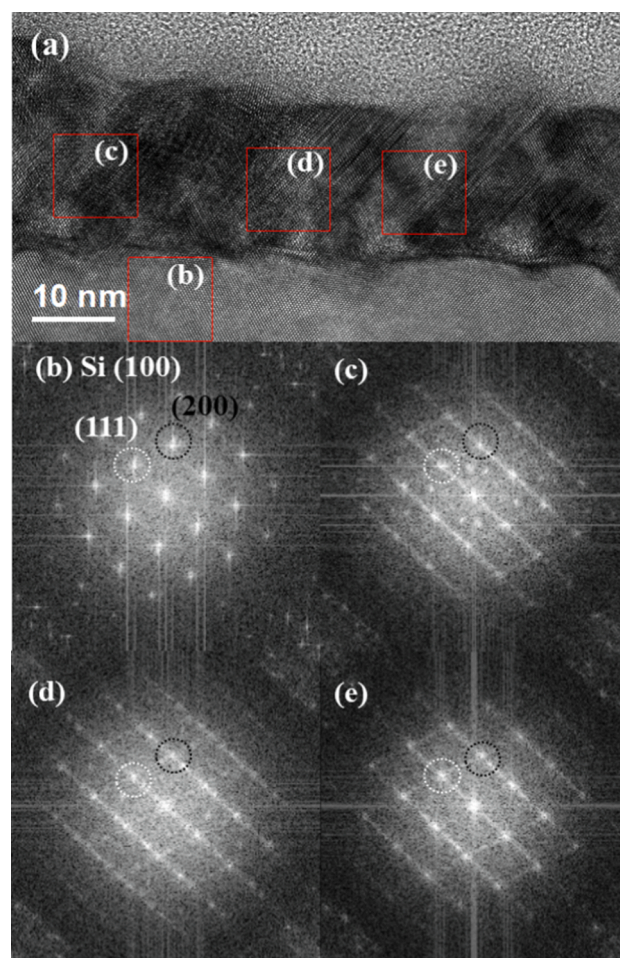


Fig. 8. HR-TEM images (a), digital diffraction patterns using FFT (b-e) of GaP Atomic H ALD on tri-TBP dry-cleaned 6°-miscut Si. Local epitaxy growth of GaP (111) in HR-TEM image, single crystal structure of Si substrate, and same orientations in diffraction patterns of GaP *epi*-layers are observed in the first GaP *epi*-layers of GaP atomic H ALD on miscut Si. White circles and black circles indicate the crystal orientation (111) and (200) respectively.

Data availability

Data will be made available on request.

Acknowledgments

The authors gratefully acknowledge funding support from the Meta Corporation via the UCSD Center for Memory and Recording Research.

Appendix A. Supplementary data

Supplementary data to this article can be found online at <https://doi.org/10.1016/j.apsusc.2023.156727>.

References

- [1] M. Ishii, S. Iwai, H. Kawata, T. Ueki, Y. Aoyagi, J. Cryst. Growth 180 (1997) 15–21.
- [2] J.A. del Alamo, Nature 479 (2011) 317–323.
- [3] D.J. Wilson, K. Schneider, S. Hönl, M. Anderson, Y. Baumgartner, L. Czornomaz, T. J. Kippenberg, P. Seidler, Nat. Photonics 14 (2020) 57–62.
- [4] A. Beyer, J. Ohlmann, S. Liebich, H. Heim, G. Witte, W. Stolz, K. Volz, J. Appl. Phys. 111 (2012) 083534.
- [5] T.J. Grassman, J.A. Carlin, B. Galiana, L. Yang, F. Yang, M.J. Mills, S.A. Ringel, Appl. Phys. Lett. 102 (2013) 142102.
- [6] D. Lee, G.D. Kwon, J.H. Kim, E. Moyaen, Y.H. Lee, S. Baik, D. Pribat, Nanoscale 6 (2014) 12943–12951.

- [7] V.V. Fedorov, O.Y. Koval, D.R. Ryabov, S.V. Fedina, I.E. Eliseev, D.A. Kirilenko, D. A. Pidgayko, A.A. Bogdanov, Y.M. Zadiranov, A.S. Goltaev, G.A. Ermolaev, A. V. Arsenin, S.V. Makarov, A.K. Samusev, V.S. Volkov, I.S. Mukhin, A.C.S. Appl. Nano Mater. 5 (2022) 8846–8858.
- [8] M.H. Weston, W. Morris, P.W. Siu, W.J. Hoover, D. Cho, R.K. Richardson, O. K. Farha, Inorg. Chem. 54 (2015) 8162–8164.
- [9] Y. Sun, D.C. Law, R.F. Hicks, Surf. Sci. 540 (2003) 12–22.
- [10] J.A. McCaulley, R.J. Shul, V.M. Donnelly, J. Vac. Sci. Technol. A 9 (1991) 2872–2886.
- [11] J.T. Boyer, A.N. Blumer, Z.H. Blumer, D.L. Lepkowski, T.J. Grassman, J. Cryst. Growth 571 (2021) 126251.
- [12] A.S. Gudovskikh, A.V. Uvarov, I.A. Morozov, A.I. Baranov, D.A. Kudryashov, E. V. Nikitina, A.A. Bukatin, K.S. Zelentsov, I.S. Mukhin, A. Levchenko, S. Le Gall, J. Kleider, J. Renew. Sustain. Energy 10 (2018) 021001.
- [13] Y. Sakuma, K. Kodama, M. Ozeki, Appl. Phys. Lett. 56 (1990) 827–829.
- [14] K. Momose, H. Yonezu, Y. Fujimoto, Y. Furukawa, Y. Motomura, K. Aiki, Appl. Phys. Lett. 79 (2001) 4151–4153.
- [15] S. Murali, N.P. Irvin, C. Zhang, R.R. King, C.B. Honsberg, 2019 IEEE 46th Photovoltaic Specialists Conference (PVSC) (2019) 1044–1048.
- [16] M. Sadeghi, S. Wang, J. Cryst. Growth 227–228 (2001) 279–283.
- [17] C. Zhang, N.N. Faleev, L. Ding, M. Boccard, M. Bertoni, Z. Holman, R.R. King, C.B. Honsberg, 2016 IEEE 43rd Photovoltaic Specialists Conference (PVSC) (2016) 1950–1953.
- [18] H. Döscher, T. Hannappel, J. Appl. Phys. 107 (2010) 123523.
- [19] M. Feifel, J. Ohlmann, J. Benick, T. Rachow, S. Janz, M. Hermlle, F. Dimroth, J. Belz, A. Beyer, K. Volz, D. Lackner, IEEE J. Photovoltaics 7 (2017) 502–507.
- [20] J.M. Olson, A. Kibbler, J. Cryst. Growth 77 (1986) 182–187.
- [21] L. Ding, C. Zhang, T.U. Nærland, N. Faleev, C. Honsberg, M.I. Bertoni, Energy Procedia 92 (2016) 617–623.
- [22] R. Cariou, W. Chen, J. Maurice, J. Yu, G. Patriarche, O. Mauguin, L. Largeau, J. Decobert, P. Roca i Cabarrocas, Sci. Reports 6 (2016) 25674.
- [23] H.C.M. Knoops, T. Faraz, K. Arts, W.M.M. Kessels, J. Vacuum Sci. Technol. A 37 (2019) 030902.
- [24] S.M. George, Chem. Rev. 110 (2010) 111–131.
- [25] S.T. Ueda, A. McLeod, D. Alvarez, D. Moser, R. Kanjolia, M. Moinpour, J. Woodruff, A.C. Kummel, Appl. Surf. Sci. 554 (2021) 149656.
- [26] A.V. Uvarov, A.S. Gudovskikh, V.N. Nevedomskiy, A.I. Baranov, D.A. Kudryashov, I.A. Morozov, J. Kleider, J. Phys. D 53 (2020) 345105.
- [27] A.L. Patterson, Phys. Rev. 56 (1939) 978–982.
- [28] S. Ng, C. Iffelsberger, J. Michalička, M. Pumera, ACS Nano 15 (2021) 686–697.
- [29] M. Alqahtani, S. Sathasivam, F. Cui, L. Steier, X. Xia, C. Blackman, E. Kim, H. Shin, M. Benamara, Y.I. Mazur, G.J. Salamo, I.P. Parkin, H. Liu, J. Wu, J. Mater. Chem. A 7 (2019) 8550–8558.
- [30] K. Yamane, T. Kobayashi, Y. Furukawa, H. Okada, H. Yonezu, A. Wakahara, J. Cryst. Growth 311 (2009) 794–797.
- [31] M. Khoury, O. Totterreau, G. Feuillet, P. Vennéguès, J. Zúñiga-Pérez, J. Appl. Phys. 122 (2017) 105108.
- [32] G. Kaneda, J. Murata, T. Takeuchi, Y. Suzuki, N. Sanada, Y. Fukuda, Appl. Surf. Sci. 113–114 (1997) 546–550.
- [33] Y. Luo (Ed.), Comprehensive Handbook of Chemical Bond Energies, CRC Press, Boca Ranton, FL, 2007.
- [34] W.L. Jolly, Modern inorganic chemistry, 2nd ed., McGraw-Hill, New York, 1991.
- [35] E. Buncel, B. Menon, J. Am. Chem. Soc. 99 (1977) 4457–4461.
- [36] F.G. Bordwell, D.J. Algrim, J. Am. Chem. Soc. 110 (1988) 2964–2968.
- [37] P. Deminskyi, C. Hsu, B. Bakhit, P. Rouf, H. Pedersen, J. Vac. Sci. Technol. A 39 (2021) 012411.
- [38] H. Kroemer, J. Cryst. Growth 81 (1987) 193–204.
- [39] I. Németh, B. Kunert, W. Stolz, K. Volz, J. Cryst. Growth 310 (2008) 1595–1601.
- [40] T. Soga, T. Jimbo, M. Umeno, J. Cryst. Growth 163 (1996) 165–170.